



# Giant electro-viscous effects in polar fluids with paraelectric–modulated antiferroelectric–ferroelectric phase sequence

Hiroya Nishikawa<sup>a</sup>, Péter Salamon<sup>b,\*</sup>, Marcell Tibor Máthé<sup>b</sup>, Antal Jákli<sup>c,d,\*</sup>, Fumito Araoka<sup>a,\*</sup>

<sup>a</sup>RIKEN Center for Emergent Matter Science (CEMS), 2-1 Hirosawa, Wako, Saitama, 351-0198, Japan

<sup>b</sup>HUN-REN Wigner Research Centre for Physics, PO Box 49, Budapest, H-1525, Hungary

<sup>c</sup>Material Science Graduate Program and Advanced Materials and Liquid Crystal Institute, Kent State University, Kent, Ohio, 44242, USA

<sup>d</sup>Department of Physics, Kent State University, Kent, Ohio, 44242, USA

**Keywords:** Ferroelectric, Antiferroelectric, Modulated antiferroelectric, Electroviscous, DIO, RM734

The recently discovered ferroelectric nematic liquid-crystal material DIO exhibits an antiferroelectric (AF) phase, characterized by a sinusoidally modulated structure between the paraelectric (P) and ferroelectric (F) nematic phases. Although these sinusoidal modulated structures associated with the P–AF–F phase sequence is commonly observed in solid ferroelectrics, their presence in soft matter systems is scarce. This study is aimed at examining the macroscopic properties of DIO, identifying unique rheological properties, such as switching between shear thinning and shear thickening behaviors at certain shear rate in the ferroelectric nematic phase. Additionally, a significant electroviscous effect is observed, with the viscosity increasing by 70 times under an ultra-low electric field of  $0.15 \text{ V } \mu\text{m}^{-1}$  at the AF–F transition.

## 1 Introduction

A small fraction of crystals with three-dimensional (3D) long-range order exhibits a unique incommensurate (IC) structure, which lacks translational periodicity in at least one direction [1]. In IC materials, internal stress may induce periodic modulation where the ratio of the modulation period to the fundamental lattice is an irrational number. If this ratio is rational, the structure is classified as commensurate (C). IC

structures often emerge through phase transitions of normal (N)–incommensurate (IC)–commensurate (C) structures phase transition sequence. This phenomenon occurs in a wide range of materials, including dielectrics [1,2], low-dimensional conductors [3], magnetic materials (magnetic helical structures) [4], surface structures [5], intercalation compounds [6], nonstoichiometric compounds [7], liquid crystals (LCs) [8], composite crystals [9], and superconducting oxides [10]. Among these, dielectrics, especially ferroelectrics, are the dominant IC materials, with typical examples including sodium nitrite ( $\text{NaNO}_2$ ) [11] and thiourea ( $\text{SC}(\text{NH}_2)_2$ ) [12]. These molecular crystals, composed of molecules with permanent dipoles, undergo spontaneous polarization owing to molecular rotation, resulting in the N–IC–C

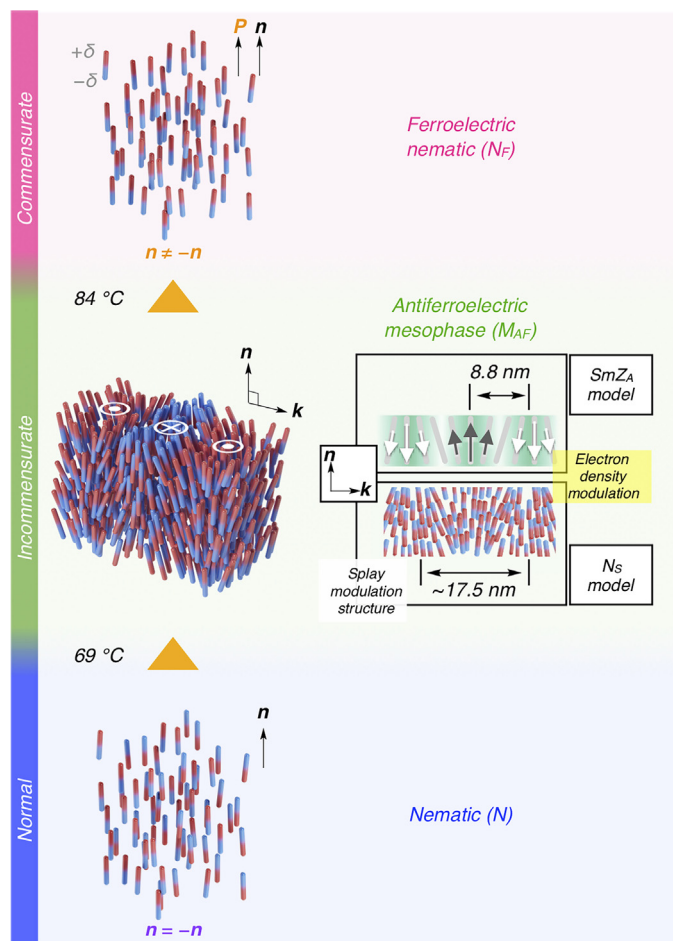
\* Corresponding authors.

E-mail addresses: [salamon.peter@wigner.hun-ren.hu](mailto:salamon.peter@wigner.hun-ren.hu) (P. Salamon), [ajakli@kent.edu](mailto:ajakli@kent.edu) (A. Jákli), [fumito.araoka@riken.jp](mailto:fumito.araoka@riken.jp) (F. Araoka).

Received 14 February 2025; Received in revised form 4 April 2025; Accepted 5 April 2025

phase transition. In these cases, N, IC, and C correspond to the paraelectric (P), sinusoidally modulated antiferroelectric (AF), and ferroelectric (F) phases, respectively.

IC structures are observed not only in solid materials but also in soft matter, such as LCs. For example, the improper ferroelectric chiral smectic ( $\text{SmC}\alpha^*$ ) phase exhibits an IC nanoscale helical pitch [8]. In this case, the phase sequence is SmA (paraelectric, P)– $\text{SmC}\alpha^*$  (ferrielectric, FI)– $\text{SmC}_A^*$  (antiferroelectric, AF), i.e., P–FI–AF. A subject of our studies is a new type of antiferroelectric liquid crystal mesophase, which was identified recently as a modulated, IC structure in the realm of the polar nematic phases. Recently, ferroelectric nematic ( $N_F$ ) LCs have garnered significant research interest owing to their excellent polarization properties (i.e., high polarization density and nonlinear optical coefficient) [13] and other unique effects, such as splay elastic softening [14], novel topology [15], thermo-rotation [16], self-propelled droplets [17], polar fiber formation [18], surface instability [19], superscreening [20], and helicity [21]. One of the archetypal  $N_F$  LCs, i.e., DIO [13a] exhibits the M1–M2–MP phase sequence upon cooling, which has been identified as a paraelectric nematic (N)–antiferroelectric smectic Z ( $\text{SmZ}_A$ )–ferroelectric nematic ( $N_F$ ) sequence (Fig. 1) [22]. This P–AF–F sequence is similar to that observed in  $\text{NaNO}_2$  [23] and  $\text{SC}(\text{NH}_2)_2$  [24], as well as in recently predicted electric-field-induced phase diagrams [22]. In the N phase of DIO, the material exhibits truly 3D fluidity (pure orientational order without positional order). In contrast, in the  $N_F$  phase, the inversion symmetry of the N director ( $\mathbf{n}$ ) is disrupted (i.e.,  $\mathbf{n} \neq -\mathbf{n}$ ), resulting in the formation of uniform domains with macroscopic polarization, whose direction can be flipped by suitable electric fields [13e]. In addition to the  $\text{SmZ}_A$  structure of the AF phase, various models for modulated antiferroelectric structures have been proposed. For instance, Mertelj et al. proposed a splay nematic ( $N_S$ ) structure [14a] with a polar-modulated nematic director field, based on splay deformation observed in another archetypal  $N_F$  LC, i.e., RM734 [13b]. Both  $\text{SmZ}_A$  and  $N_S$  models (referred to as antiferroelectric mesophases ( $M_{AF}$ ) herein), are similar in that the nematic director ( $\mathbf{n}$ ) and polarization ( $\mathbf{P}$ ) vectors are oriented in the same direction within several nanometers thick local-polar slabs, with alternating polarization directions in adjacent slabs, resulting in an antiferroelectric structure [22,25]. In the  $\text{SmZ}_A$  model, the periodic modulation of electron density presents in along the modulation wave vector ( $\mathbf{k}$ ), which is perpendicular to  $\mathbf{n}$  ( $\mathbf{n} \perp \mathbf{k}$ ), with the periodicity of 8.8 nm. For the  $N_S$  model, there is a modulation period with nm size of the splay structure, which is biaxial and can be described by the director and the splay wave vector  $\mathbf{k}_s$  ( $\mathbf{n} \perp \mathbf{k}_s$ ). Note that both  $\text{SmZ}_A$  and  $N_S$  has electron density modulation as the periodically varying splays lead to periodically charge density ( $\nabla P = -\rho$ ). In the  $\text{SmZ}_A$  model, mass density variation is even considered. Nacke et al. proposed a model in which the distribution of dipole moments with opposite signs increases continuously along the wave vector ( $\mathbf{k}$ ) while traversing slabs, until the polarization direction is completely flipped [26]. This suggests that the  $M_{AF}$  phase exhibits a sinusoidally modulated antiferroelectric structure, similar to the IC phase observed in the  $\text{NaNO}_2/\text{SC}(\text{NH}_2)_2$  system.



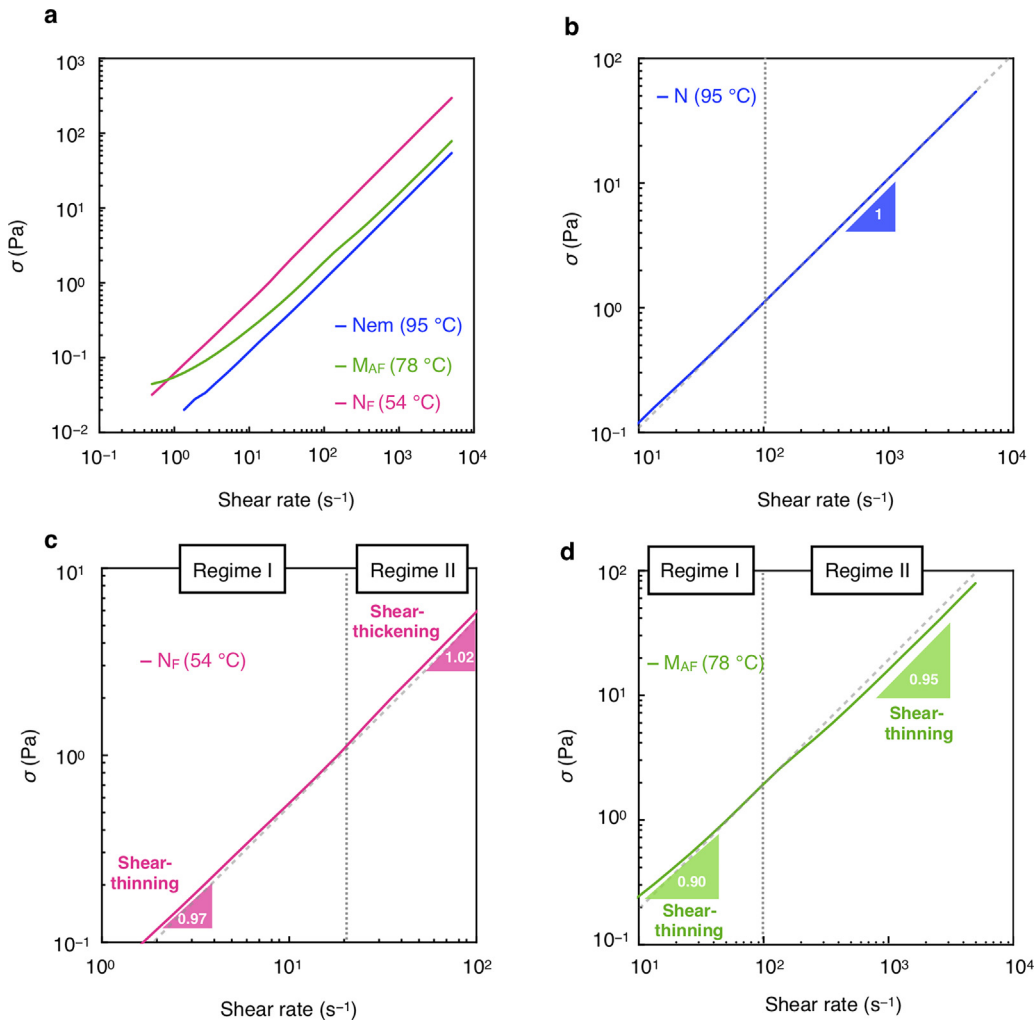
**Fig. 1**

Illustration of the normal (N) – incommensurate ( $M_{AF}$ ) – commensurate ( $N_F$ ) phase sequence in DIO.  $+\delta$  and  $-\delta$  denote plus and minus electrical charges at one end of a molecule, respectively.  $\mathbf{n}$ ,  $\mathbf{k}$  and  $\mathbf{P}$  denote orientation director, modulation wave vector and polarization director, respectively. In the  $M_{AF}$  phase, the label of  $\odot$  and  $\otimes$  represent an opposite direction of  $\mathbf{P}$  in a layer plane (not shown in figure), respectively. For the structure of  $M_{AF}$  phase, antiferroelectric smectic Z ( $\text{SmZ}_A$ ) and splay nematic ( $N_S$ ) models are proposed. In the  $\text{SmZ}_A$  model, the electron density in green shadowed area is denser than that in white shadow area.

The appearance of antiferroelectric phases with sinusoidally modulated structures in soft matter systems is extremely rare, and the macroscopic properties associated with phase transitions remain understudied. Here we report rheological studies of DIO and find unique properties, such as switching between shear thinning and shear thickening behavior at certain shear rate in the ferroelectric nematic phase, and an order of magnitude larger electro-viscous effect in DIO with P–AF–F sequence than for RM734 with P–F transition.

## 2 Results and discussion

In LCs, the director rotation and flow velocity gradient are coupled, and the flow viscosity depends on the director ( $\mathbf{n}$ ) orientation. For nematic LCs, Miesowicz's viscosity coefficients  $\eta_b$  ( $\eta_c$ ) describe the viscosity when the director is parallel (perpendicular) to the flow velocity and perpendicular (parallel) to the velocity gradient:  $\eta_b: \mathbf{v} \parallel \mathbf{n}, \nabla \mathbf{v} \perp \mathbf{n}$ ;  $\eta_c: \mathbf{v} \perp \mathbf{n}, \nabla \mathbf{v} \parallel \mathbf{n}$ .  $\eta_b$  and  $\eta_c$



**Fig. 2**

(a) Stress as a function of shear rate in the N,  $M_{AF}$  and  $N_F$  phases. Enlarged panel for N (b),  $M_{AF}$  (c) and  $N_F$  (d) phases.

correspond to the lowest and highest shear viscosity, respectively [27]. Additionally, an intermediate viscosity,  $\eta_a$ , arises when the director is perpendicular to the shear plane:  $\eta_a: v \perp n, \nabla v \perp n$ . Films of rod-like nematic LCs exhibit shear-thinning behavior [28], with the extent of thinning depending on the film thickness. In general, the relationship between the shear stress and shear rate can be described using the power-law model [29]:

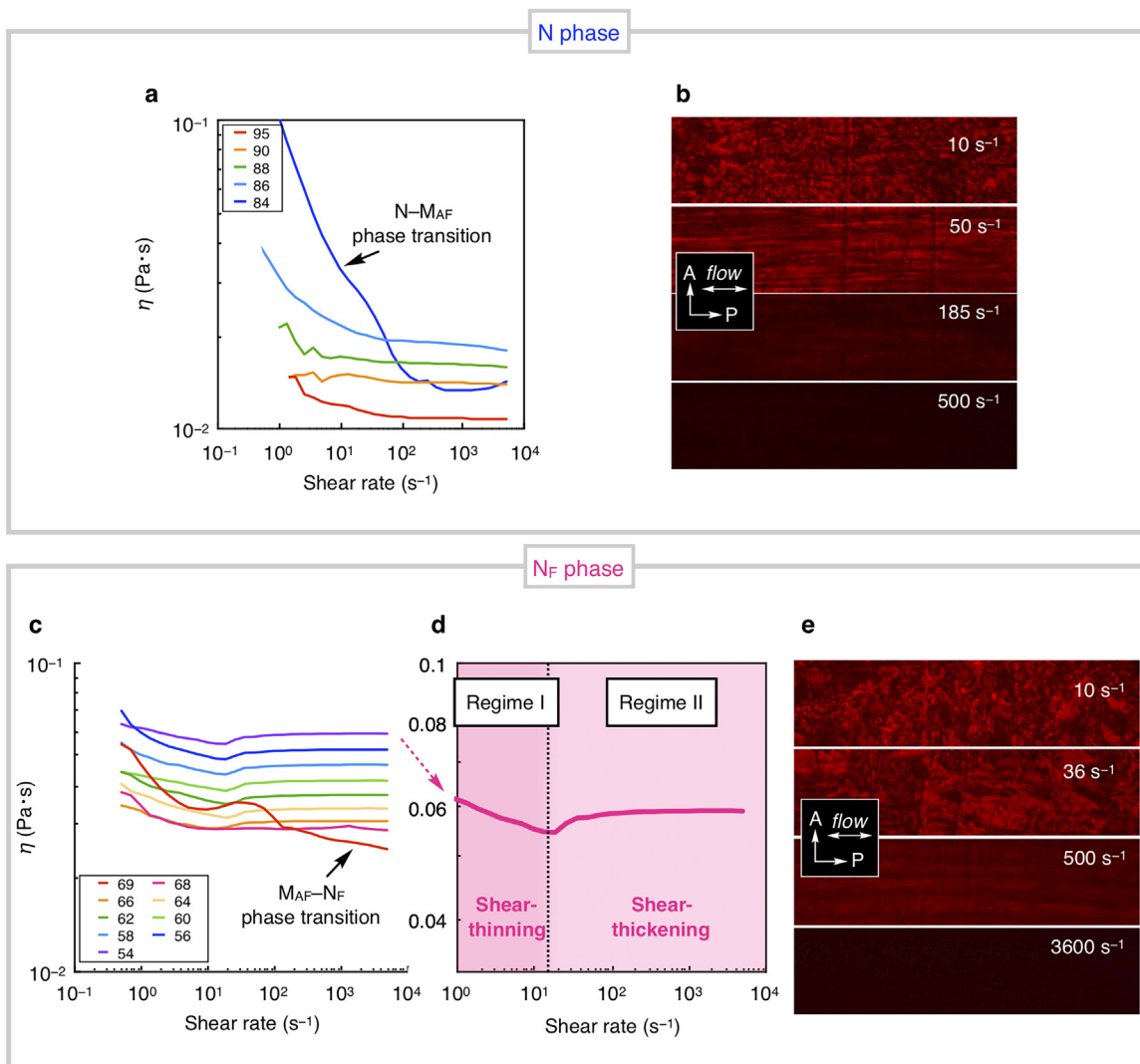
$$\sigma = \kappa(\dot{\gamma})^\alpha, \quad (1)$$

where  $\sigma$ ,  $\kappa$ ,  $\dot{\gamma}$ , and  $\alpha$  denote the shear stress, flow consistency index, shear rate, and flow behavior index, respectively. For Newtonian fluids,  $\alpha = 1$ , whereas shear-thinning and shear-thickening behaviors are observed when  $\alpha < 1$  and  $\alpha > 1$ , respectively. Viscosity is defined as  $\eta = \sigma / \dot{\gamma}$ . Fig. 2a displays the dependence of shear stress ( $\sigma$ ) on shear rate in the N,  $M_{AF}$ , and  $N_F$  phases, measured under steady-shear conditions. In the N phase, the shear stress is proportional to the shear rate (above 10–100  $s^{-1}$ ), indicating Newtonian fluid behavior (Fig. 2b). Similarly, Fig. 3a shows that the Newtonian behavior is true only for shear rate above 10–100  $s^{-1}$ , and the shear rate dependence above 100  $s^{-1}$  was relatively weak. Below these rates, shear thinning occurs.

This is because of the transition from flow-induced to surface alignment, which is characterized by the parameter  $e_1$  describing the thickness of the boundary layer, where the alignment changes from the one dictated by the surface alignment to the one defined by the flow alignment angle. [27] Thus,  $e_1$  is expressed by

$$e_1 = \sqrt{\frac{K}{\eta \dot{\gamma}}}, \quad (2)$$

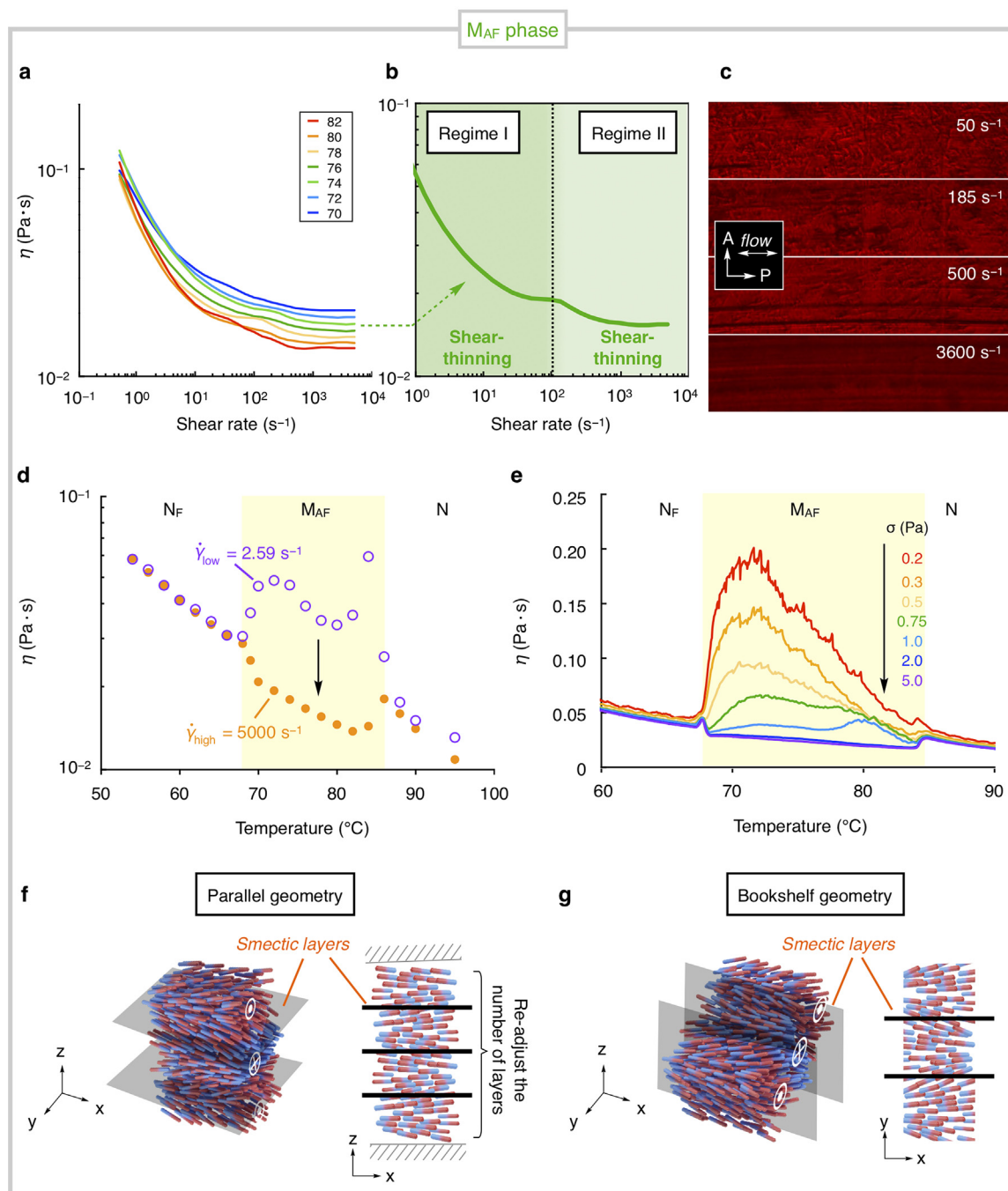
where  $e_1$ ,  $K$ ,  $\eta$ ,  $\dot{\gamma}$  are the thickness parameter, elastic constant, viscosity and shear rate, respectively. Thus, the value of  $e_1$  decreases at increasing shear rate. In contrast, the  $N_F$  phase exhibits different slopes at the crossover point ( $\dot{\gamma} = 20 s^{-1}$ ). Thus,  $n = 0.97 < 1$  and  $n = 1.02 > 1$  in Regimes I and II, representing shear-thinning and shear-thickening behaviors, respectively (Fig. 2c). As shown in Fig. 2d, the  $M_{AF}$  phase exhibits  $\sigma \propto \dot{\gamma}^{0.90}$  and  $\sigma \propto \dot{\gamma}^{0.95}$  in Regimes I and II, respectively, representing shear thinning. Fig. 3 shows the viscosity as a function of the shear rate in the N and  $N_F$  phases. In the N phase, at 95 °C and  $\dot{\gamma} = 5 s^{-1}$ , the viscosity is  $\eta = 12 mPa \cdot s$  (Fig. 3a). At increasing shear rates between 100 and 5000  $s^{-1}$ , the viscosity decreases to  $\eta = 10.8 mPa \cdot s$ . Near the N– $M_{AF}$  phase

**Fig. 3**

Apparent viscosity as a function of shear rate and the corresponding POM images during shearing with different shear rate in the N (a,b) and  $N_F$  (c,d,e) phases. The POM images were taken at 95 °C (b) and 60 °C (e). (d) Highlighted profile recorded at 54 °C.

transition,  $\eta$  increases to 39 mPa·s at low shear rates, with steady-state conditions attained at high shear rates. Polarized optical microscopy (POM) images (Fig. 3b) confirm that the director reorients along the flow direction at higher shear rate. The grainy texture observed at low  $\dot{\gamma}$  turns to homogeneous over few hundred  $s^{-1}$  indicating the alignment by the shear. Note that our experimental apparatus lacked orienting layers, and also because of the large thickness (80  $\mu\text{m}$ ), the initial director field was randomly oriented in the sample plane, which is observed as the grainy POM textures seen at low shear rates (Figs. 3 and 4). Before each measurement, to homogenize the sample, and to avoid any transient behavior, we applied preshearing at 10 Pa shear stress for 10 min. After the relaxation of the preshearing, the sample became again unoriented as presented in the POM textures, therefore the effect of shear alignment has not been preserved after ceasing the flow. Similar to the N phase, shear-thinning behavior is also observed at low shear rates ( $\dot{\gamma} < 20 s^{-1}$ ) in  $N_F$  phase (Fig. 3c and d). Comparing to the N phase, the sequence of POM textures in the

$N_F$  phase is similar, but shifted towards higher shear rates (Fig. 3e), owing to the higher viscosity (59 mPa·s at  $T = 54$  °C). Notably, the viscosity increases in the range  $20 s^{-1} \leq \dot{\gamma}$  reaching a nearly constant value of  $\sim 60$  mPa·s at higher shear rates. In this regime, a uniform texture is observed (Fig. 3e). The Newtonian behavior at high shear rates in the nematic phase likely corresponds to the negligible transient alignment near the surface and the resulting uniform alignment. The transient increase in viscosity in the  $N_F$  phase above  $20 s^{-1}$  is likely related to the director realignment and generation of polar defects, a distinct characteristic of the  $N_F$  phase. The experimental data does not provide clear evidence on the presence of polar defects, and their effect on the rheological properties. POM images, however, show larger areas or domains with different brightness in the shear thickening regime of the  $N_F$  phase (see Fig. 3e:  $36 s^{-1}$ ), which may be a polar domain structure responsible for increased resistance against flow leading to shear thickening. In the N and  $N_F$  phases, at high shear rates, the texture appears dark (Fig. 3b and e), with the polarizer axis parallel to the

**Fig. 4**

(a) Apparent viscosity as a function of shear rate at different temperatures. (b) Highlighted profile recorded at 78 °C; (c) The corresponding POM images taken at 78 °C during shearing with different shear rate; (d) Apparent viscosity vs temperature recorded at high (5000 s<sup>-1</sup>) and low (2.59 s<sup>-1</sup>) shear rate; (e) Apparent viscosity vs temperature recorded at various shear stress ranging between 0.2 and 5.0 Pa. Schematic illustration of M<sub>AF</sub> phase (parallel (f) and bookshelf (g) geometries), in which each molecule lies on the substrate and flow along shear direction. For the parallel and the bookshelf cases, the smectic layers are parallel (f) and perpendicular (g) to the substrate, respectively. In the parallel geometry, layers cannot glide near the plate, since there are always slight inhomogeneities in the film thickness. In the bookshelf geometry, the plate and the layer are orthogonal, and shear along the layer is easy. In both (f) and (g), the shear plane is in the z-x plane.

flow direction. This indicates that the flow orients the director to be in the shear plane, which is characteristic of flow-aligning behavior in nematic LCs [30]. In the flow aligning cases of the N and N<sub>F</sub> phase, in the high shear rate limit with no applied E-field, the measured effective viscosity approaches the Miesowicz

viscosity  $\eta_b$  but being slightly higher than that due to the small shear alignment angle (typically 5°–15° [27]).

In the M<sub>AF</sub> phase, the viscosity exceeds 100 mPa·s, which is six and two times that in the N and N<sub>F</sub> phases, respectively (Fig. 4a). As shown in Figs. 2d, 4a–c, the M<sub>AF</sub> phase exhibits two

types of shear-thinning behavior: regime I and II with apparently distinct shear rate dependence of the viscosity. This property may be attributable to tumbling motion, rather than the shear alignment observed in the N and N<sub>F</sub> phases, typically found in smectic LCs [31]. The temperature dependence of apparent viscosity under constant shear rate and stress was evaluated. As shown in Fig. 4d, in the N and N<sub>F</sub> phases, the apparent viscosity increases with decreasing temperature, independent of the shear rate. In contrast, in the M<sub>AF</sub> region, the viscosity is higher at low shear rate of  $\dot{\gamma} = 2.59 \text{ s}^{-1}$  but decreases below the values observed for the N and N<sub>F</sub> phases at high shear rates ( $\dot{\gamma} = 5000 \text{ s}^{-1}$ ). This difference also arises under different stress conditions, where the viscosity decreased with increasing stress from 0.2 to 5.0 Pa. These results show that a distinct structure exists in the M<sub>AF</sub> phase, as discussed in the introduction. This could correspond either to an antiferroelectric lamellar order with a periodicity of  $\sim 17.5 \text{ nm}$ , including 8.8-nm-thick layer pairs with opposite ferroelectric polarization, or a modulated splay-nematic phase with  $\sim 17.5 \text{ nm}$  periodicity [22,25]. Under confinement, the M<sub>AF</sub> phase can adopt two geometries, wherein the layers align either normal (“bookshelf”) or parallel to the plates. At low shear rates, where the smectic structure is not completely destroyed, the system likely selects an optimal structure for flow during shearing. For example, if the parallel geometry of M<sub>AF</sub> phase was adopted, each lamellar layer may glide along the shear direction (Fig. 4f). However, this is not necessarily the optimal geometry, as the two boundary plates are rarely perfectly parallel. Therefore, the layers near the substrates cannot glide and must adjust their thickness, which is energy-intensive. In contrast, in the bookshelf alignment, the boundary of the layers normal to the substrates may exhibit any shape (Fig. 4g). Consequently, the parallel alignment is associated with higher viscosity, and the bookshelf alignment corresponds to lower viscosity. Based on these findings, we propose a mechanism for the dual shear-thinning behavior in Regimes I and II for the M<sub>AF</sub> phase. The shear-thinning behavior in Regime I reflects the deformation of the lamellar layer in the parallel geometry, which corresponds to high viscosity. Subsequently, the geometry reorients to the bookshelf alignment with lower viscosity, reflecting the additional shear-thinning behavior in Regime II. At high shear rates and stress in the M<sub>AF</sub> phase, the rheology exhibits two key features. First, in contrast to the N and N<sub>F</sub> phases, the optical texture under crossed polarizers (Fig. 4c) remains bright, indicating the presence of a significant director component perpendicular to the shear plane, characteristic of tumbling nematics [30]. Second, the M<sub>AF</sub> phase demonstrates lower effective viscosity relative to the N and N<sub>F</sub> phases at extremely high shear rates (Fig. 4d). Similar results have been obtained in the nematic phase of 8CB, where viscosity decreases as the system transitions from flow-aligning to tumbling at high shear rates [32].

Next, we investigated the effect of the  $E$ -field on viscosity across the three phases. The effect of flow and  $E$ -field are conflicting with each other. Thus, when the shear rate is sufficiently small, the vertical alignment of the molecules (with positive dielectric anisotropy) can be realized under the  $E$ -field, thereby increasing the apparent viscosity. In the high- $E$ -field limit, the viscosity is expected to approach the high Miesowicz viscosity, namely

$\eta_c$ . In ferroelectric LCs, the induction of flow or deformation can be easily tuned owing to the coupling between spontaneous polarization and the  $E$ -field (i.e.,  $P \times E$ ). As shown in Fig. S1a, in the N phase, the apparent viscosity under the  $E_{DC}$ -field is smaller than that under the  $E_{AC}$ -field. This difference is attributable to DC ionic screening, which is negligible in  $E_{AC}$ -fields. In contrast, in the M<sub>AF</sub> and N<sub>F</sub> phases, the application of  $E_{DC}$  is more effective in reorienting the director (Figs S1b and S1c), attributable to the polar interaction between the electric field and polarization of these phases. Fig. 5a and c show the dependence of apparent viscosity on  $E_{AC}$ - and  $E_{DC}$ -fields under constant shear stress ( $\sigma = 20 \text{ Pa}$ ) in the N/M<sub>AF</sub> and M<sub>AF</sub>/N<sub>F</sub> regimes, respectively. When  $E = 0.15 \text{ V } \mu\text{m}^{-1}$  is applied, the viscosity in the N phase doubles (from 10 to 20 mPa·s at 90 °C), whereas in the N<sub>F</sub> phase, it increases eightfold (from 30 to 240 mPa·s at 64 °C). In the M<sub>AF</sub> phase, although  $E = 0.15 \text{ V } \mu\text{m}^{-1}$  is inadequate to saturate the viscosity, the viscosity dramatically increases near the M<sub>AF</sub>–N<sub>F</sub> phase transition. Specifically, at 70 °C, the viscosity increases 70-fold, from 18.6 mPa·s to 1.29 Pa·s. Fig. 6a shows the zero-field viscosity and  $E$ -field-induced viscosity as functions of temperature under  $\dot{\gamma} = 100 \text{ s}^{-1}$ . The kink points of viscosity change at the N–M<sub>AF</sub> phase transition appear at the same temperature, regardless of  $E$ -field application. In contrast, at the M<sub>AF</sub>–N<sub>F</sub> phase transition, the kink point temperature under the  $E$ -field is 2 °C higher than that under the zero field. This suggests that the M<sub>AF</sub> phase transforms to the N<sub>F</sub> phase upon the application of the  $E$ -field, i.e., the sufficiently large  $E$ -field induces phase transition from an antiferroelectric state to a ferroelectric state. The induction of the N<sub>F</sub> phase from the isotropic phase upon  $E_{DC}$ -field application has been observed for other compounds as well [33].

Next, we examined viscosity changes at the N–M<sub>AF</sub> and M<sub>AF</sub>–N<sub>F</sub> phase transitions under the  $E$ -field. The relative percentage enhancement of viscosity as a percentage is defined as

$$\eta_{\%} = \frac{\eta(E = E_s) - \eta_0}{\eta_0} \times 100, \quad (3)$$

where  $\eta(E = E_s)$ , and  $\eta_0$  denote the saturated viscosity at a high  $E$ -field and the initial viscosity under zero field, respectively. Kumar et al. reported a significant  $\eta_{\%} \sim 700\%$  at the N–N<sub>F</sub> phase transition in RM734 [35]. Our results closely match these findings ( $\eta_{\%} \sim 800\%$ ) for RM734 (Fig. 6d and Figs S2a and S2b). However, at the M<sub>AF</sub>–N<sub>F</sub> phase transition for DIO,  $\eta_{\%} \sim 7000\%$  (Fig. 6c), i.e., an order of magnitude larger than that at the N–N<sub>F</sub> phase transition for RM734. In RM734, during the N–N<sub>F</sub> phase transition, the ferroelectric domains develop rapidly resulting in a notable electroviscous effect [34]. Near the M<sub>AF</sub>–N<sub>F</sub> phase transition of DIO, the viscosity exhibits critical-like behavior in the presence of  $E_{DC}$ -field as seen in Fig. 6a. We think that in a narrow temperature range around the M<sub>AF</sub>–N<sub>F</sub> phase transition, the ferroelectric and antiferroelectric phases can coexist, and this situation may cause a difference in the behavior compared to the homogeneous neat phases. One aspect to consider is the multiphase flow of the system. A possible scenario is that the higher base viscosity of the M<sub>AF</sub> phase is increased by ferroelectric clusters, inclusions, which are more sensitive to the  $E$ -field. A comprehensive explanation of this effect requires further theoretical/modeling efforts, which will be the subject of future

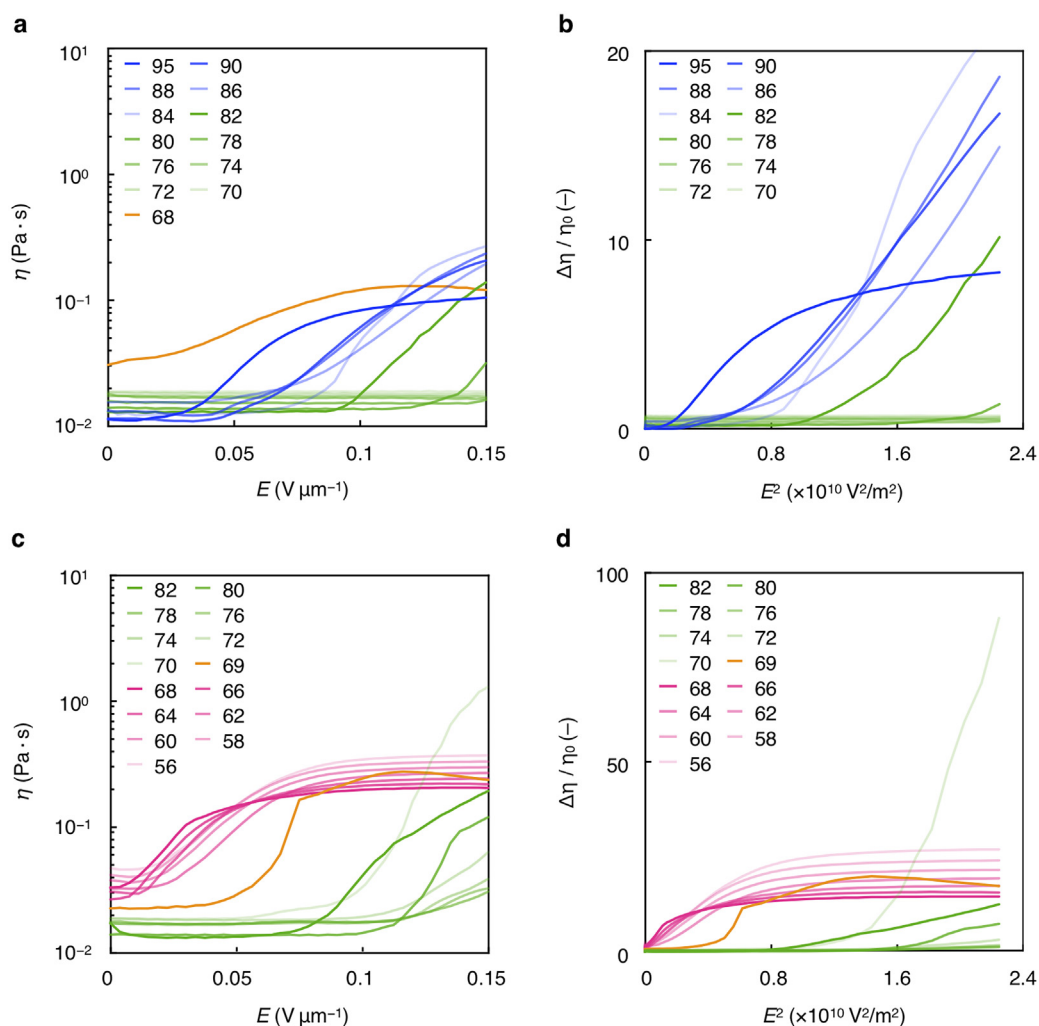


**Fig. 5**

*E*-field dependence of the apparent viscosity measured at constant shear rate ( $100 \text{ s}^{-1}$ ) by applying (a): 1 kHz  $E_{AC}$ -field; (c):  $E_{DC}$ -field in the N (blue line),  $M_{AF}$  (green line), and  $N_F$  (magenta line) phases. (b,d):  $\Delta\eta/\eta_0$  vs  $E^2$  profiles obtained from data in the panel (a) and (c), respectively. Note that during the  $M_{AF}$ – $N_F$  phase transition, the light transmittance was almost zero because the director reoriented along the *E*-field.

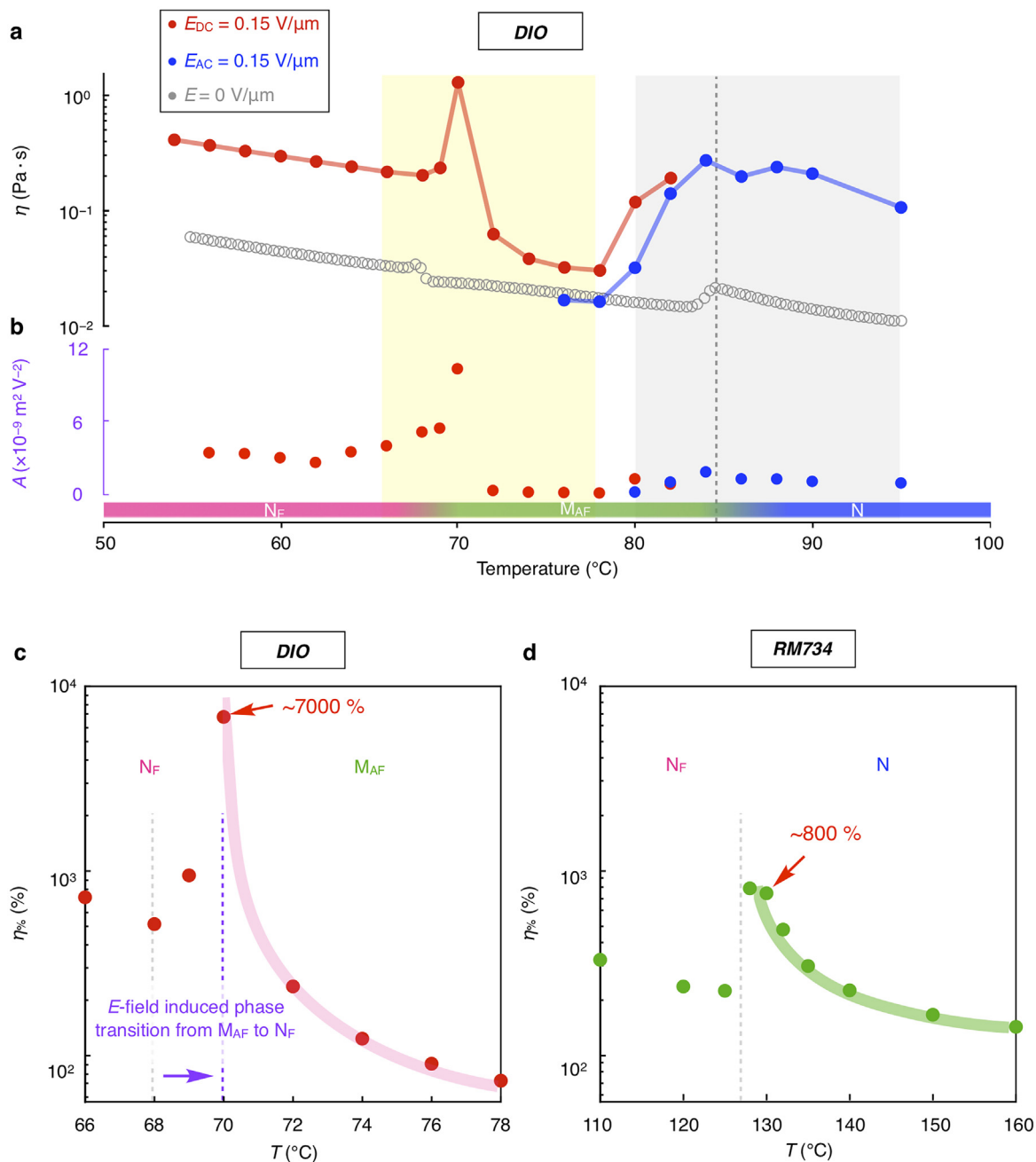
studies and beyond the scope of the present work. The application of an *E*-field in the  $M_{AF}$  phase may also induce the ferroelectric phase, effectively frustrating and hardening the material as it transitions to the  $N_F$  phase. This is consistent with the 2 °C shift of the transition temperature when an *E*-field is applied (Fig. 6c). Recently, precise differential scanning calorimetry measurements have confirmed the presence of the  $M_{AF}$  phase even in RM734 [35]. However, the dramatic electroviscous effect at the  $M_{AF}$ – $N_F$  phase transition is not observed in RM734. This difference may be attributable to various factors, specifically, the temperature range of the  $M_{AF}$  phase is below 1 K, the molar transition enthalpy between  $M_{AF}$  and  $N_F$  is approximately half that of DIO, and the intermolecular interactions before and after the transition are weaker than those of DIO. The electro-rheological properties of the studied material can be described using the following phenomenological equation:

$$\eta = \eta_0(1 + AE^2), \quad (4)$$

where  $\eta_0$ ,  $A$ , and  $E$  denote the bulk viscosity, viscoelectric coefficient, and *E*-field, respectively.  $A$  can be defined as

$$\frac{\eta(E) - \eta_0}{\eta_0} = \frac{\Delta\eta}{\eta_0} = AE^2. \quad (5)$$

Thus,  $A$  can be calculated from the slope of the relative viscosity  $(\eta(E) - \eta_0)/\eta_0$  vs.  $E^2$ . For our system,  $A$  in the N,  $M_{AF}$ , and  $N_F$  phases was estimated using Eq. (5). The relative viscosity vs.  $E^2$  curve is shown in Fig. 5b and d. We derived the slope from the linear region. The estimated values were as follows:  $A_N$  (95 °C) =  $0.91 \times 10^{-9}$ ,  $A_{MAF}$  (74 °C) =  $0.16 \times 10^{-9}$ , and  $A_{NF}$  (60 °C) =  $3.0 \times 10^{-9} \text{ V}^2 \text{ m}^{-2}$  (Fig. 6b). For RM734,  $A_N$  (150 °C) =  $0.08 \times 10^{-9}$  and  $A_{NF}$  (110 °C) =  $3.0 \times 10^{-9} \text{ V}^2 \text{ m}^{-2}$  under the same conditions (Fig. S2c and S2d). Notably, the value of  $A_{NF}$  for DIO and RM734 is 5–7 orders of magnitude greater than that exhibited by common organic polar fluids [36].

**Fig. 6**

(a): Temperature dependence of the apparent viscosity under constant ( $\sigma = 20 \text{ Pa}$ ) shear stress without/with  $E$ -field ( $E_{DC} = E_{AC} = 0.15 \text{ V } \mu\text{m}^{-1}$ ,  $f(E_{AC}) = 1 \text{ kHz}$ ); (b): Visco-electric constant  $A$  as a function of temperature; (c):  $\eta\%$  vs  $T$  for DIO; (d):  $\eta\%$  vs  $T$  for RM734.

### 3 Conclusion

We investigated the rheological properties and electroviscous effects of the polar fluid DIO in the  $N$ ,  $M_{AF}$ , and  $N_F$  phases, corresponding to a P–AF–F system. At high shear rates, the  $N_F$  phase exhibited an increase in effective viscosity (shear thickening) owing to the generation of polar defects. In the  $M_{AF}$  phase, two types of shear-thinning modes were observed at low and high shear rates, and the apparent viscosity responses to increasing shear rate and shear stress were remarkable. The viscosity significantly decreased by this two-stage shear-thinning,

which may be attributable to two potential mechanisms: the transition from the parallel arrangement of the  $M_{AF}$  phase to the bookshelf arrangement, and the shift from flow orientation to tumbling behavior. Finally, we demonstrated that an ultra-low  $E$ -field ( $0.15 \text{ V } \mu\text{m}^{-1}$ ) induced an extremely large electroviscous effect (70-fold increase) near the modulated antiferroelectric–ferroelectric phase transition. The effect was an order of magnitude larger than that observed in RM734 near the paraelectric–ferroelectric phase transition. We believe that this unique electroviscous effect can be leveraged to develop an

electrical smart brake suitable for smart cities and smart mobility solutions.

## 4 Experimentals

### 4.1 Materials and general measurements

The NF LC material (DIO) was synthesized and recrystallized twice from dichloromethane/n-hexane mixture in our laboratory. The NF LC material (RM734) was purchased from INSTEC Inc. and used without any purifications. The rheological properties of the NF LCs were measured by an Anton Paar MCR502 rheometer by using a parallel plate measuring system (PP25/DI/TI, diameter ~25 mm and PP50/DI/TI-SN38600, diameter ca. 50 mm), as shown in Fig. S3a. The sample thickness was fixed to be 80  $\mu\text{m}$  for all experiments. All measurements were conducted on cooling from the isotropic phase under N<sub>2</sub> gas stream to reduce sample degradation.

### 4.2 Measurement system #1

The rheometer was equipped with the Anton Paar P-PTD 200/SS/DI dielectric module to investigate the electro-viscous effect in LC phases. We turned on potential difference between the fixed bottom and the rotating measuring system by using the signals of a TiePie Handyscope HS3 device amplified by an FLC F10A amplifier. The electrical contact to the rotating part was achieved by a needle orbiting in a 3D printed circular pool filled with 10 % aqueous NaCl solution to eliminate friction. To avoid water evaporation from the electrolyte we applied a covering layer of silicone oil (Wacker Silicone Fluids AK M20, viscosity: 20 mPa·s@r.t.). We confirmed that the torque from the fluid electrical contact was too small to affect any measurement.

### 4.3 Measurement system #2

To observe polarized optical microscopic (POM) textures without and with *E*-field, we used the Anton Paar rheo-microscope module with a custom-made parallel plate measuring system made of an indium-tin-oxide (ITO) coated glass (diameter: ca. 25 mm), and a custom-made monochromatic LED light source (wavelength: 660 nm) for transmission mode (Fig. S3b).

## Declaration of competing interest

The authors declare that they have no known competing financial interests or personal relationships that could have appeared to influence the work reported in this paper.

## Data availability

Data will be made available on request.

## CRedit authorship contribution statement

**Hiroya Nishikawa:** Writing – original draft, Visualization, Methodology, Investigation, Formal analysis, Data curation, Conceptualization. **Péter Salamon:** Writing – review & editing, Supervision, Software, Resources, Project administration, Methodology, Investigation, Funding acquisition, Conceptualization. **Marcell Tibor Máthé:** Writing – review & editing, Methodology. **Antal Jáklí:** Writing – review & editing, Supervision. **Fumito Araoka:** Writing – review &

editing, Supervision, Resources, Project administration, Funding acquisition.

## Acknowledgements

This work was financially supported by the Hungarian National Research, Development, and Innovation Office under grants NKFIH FK142643 and 2023-1.2.1-ERA\_NET-2023-00008 (P.S.), the US National Science Foundation under grant DMR-2210083 (A.J.). The work was also supported by the János Bolyai Research Scholarship of the Hungarian Academy of Sciences (HAS) (BO/00294/22/11; P.S.). This work was partially supported by JSPS KAKENHI (JP22K14594; H.N., 23K17341, JP21H01801; F.A.), RIKEN Special Postdoctoral Researchers (SPDR) fellowship (H.N.), FY2022 RIKEN Incentive Research Projects (H.N.), and JST CREST (JPMJCR17N1; F.A.) and JST SICORP EIG CONCERT-Japan (JPMJSC22C3; F.A.).

## Supplementary materials

Supplementary material associated with this article can be found, in the online version, at [doi:10.1016/j.giant.2025.100356](https://doi.org/10.1016/j.giant.2025.100356).

## References

- [1] H.Z. Cummins, Experimental studies of structurally incommensurate crystal phases, *Phys. Rep.* 185 (1990) 211, doi:10.1016/0370-1573(90)90058-A.
- [2] R. Blinc, A.P. Levanyuk, *Incommensurate Phases in Dielectrics*, first ed., North-Holland, 1986.
- [3] J.A. Wilson, F.J. Disalvo, S. Mahajan, Charge-density waves and superlattices in the metallic layered transition metal dichalcogenides, *Adv. Phys.* 24 (1975) 117–120, doi:10.1080/00018737500101391.
- [4] J. Rossat-Mignod, Magnetic structures of rare earth intermetallics, *J. Phys. Colloquies* 40 (1979) C5-95–C5-100, doi:10.1051/jphyscol:1979535.
- [5] T. Aruga, Charge-density waves on metal surfaces, *J. Phys. Condens. Matter* 14 (2002) 8393, doi:10.1088/0953-8984/14/35/310.
- [6] R. Clarke, N. Caswell, S.A. Solin, P.M. Horn, Positional and orientational correlations in the graphite intercalate C<sub>24</sub>Cs, *Phys. Rev. Lett.* 43 (1979) 2018, doi:10.1103/PhysRevLett.43.2018.
- [7] A. Yamamoto, Modulated structure of wustite (Fe<sub>1-x</sub>O) (three-dimensional modulation), *Acta Cryst.* B38 (5) (1982) 1451–1456, doi:10.1107/S056774088200613X.
- [8] A. Cady, X.F. Han, D.A. Olson, H. Orihara, C.C. Huang, Optical characterization of a nanoscale incommensurate pitch in a new liquid-crystal phase, *Phys. Rev. Lett.* 91 (2003) 125502, doi:10.1103/PhysRevLett.91.125502.
- [9] M. Onoda, K. Kato, Structure of the incommensurate composite crystal (PbS)<sub>1.12</sub>VS<sub>2</sub>, *Acta Cryst.* B46 (1990) 487–492, doi:10.1107/S0108768190003950.
- [10] T.M. Shaw, S.A. Shivashankar, S.J. La Placa, J.J. Cuomo, T.R. McGuire, R.A. Roy, K.H. Kelleher, D.S. Yee, Incommensurate structure in the Bi-Sr-Ca-Cu-O 80-K superconductor, *Phys. Rev. B* 37 (1988) 9856, doi:10.1103/PhysRevB.37.9856.
- [11] S. Tanisaki, Microdomain structure in paraelectric phase of NaNO<sub>2</sub>, *J. Phys. Soc. Jpn.* 16 (1961) 579, doi:10.1143/JPSJ.16.579.
- [12] Y. Shiozaki, Satellite X-ray scattering and structural modulation of thiourea, *Ferroelectrics* 2 (1971) 245–260, doi:10.1080/00150197108234099.
- [13] a) H. Nishikawa, K. Shiroshita, H. Higuchi, Y. Okumura, Y. Haseba, S. Yamamoto, K. Sago, H. Kikuchi, A fluid liquid-crystal material with highly polar order, *Adv. Mater.* 29 (2017) 1702354, doi:10.1002/adma.201702354; b) R.J. Mandel, S.J. Cowling, J.W. Goodby, A nematic to nematic transformation exhibited by a rod-like liquid crystal, *Phys. Chem. Chem. Phys.* 19 (2017) 11429–11435, doi:10.1039/C7CP00456G; c) X. Chen, E. Korblova, D. Dong, X. Wei, R. Shao, L. Radzihovsky, M.A. Glaser, J.E. MacLennan, D. Bedrov, D.M. Walba, N.A. Clark, First-principles experimental demonstration of ferroelectricity in a thermotropic nematic liquid crystal: polar domains and striking electro-optics, *Proc. Natl. Acad. Sci. U.S.A.* 117 (25) (2020) 14021–14031, doi:10.1073/pnas.2002290117; d) A. Manabe, M. Bremer, M. Kraska, Ferroelectric nematic phase at and below room temperature, *Liq. Cryst.* 48 (2021) 1079–1086, doi:10.1080/02678292.2021.1921867; e) N. Sebastián, M. Čopič, A. Mertelj, Ferroelectric nematic liquid-crystalline phases, *Phys. Rev. E* 106 (2022) 021001, doi:10.1103/PhysRevE.106.021001.
- [14] a) A. Mertelj, L. Čmok, N. Sebastián, R.J. Mandel, R.R. Parker, A.C. Whitwood, J.W. Goodby, M. Čopič, Splay nematic phase, *Phys. Rev. X* 8 (2018) 041025; b) N. Sebastián, L. Čmok, R.J. Mandel, M.R. De La Fuente, I. Drevenšek Olenik, M. Čopič, A. Mertelj, Ferroelectric-ferroelastic phase transition in a nematic liquid crystal, *Phys. Rev. Lett.* 124 (2020) 037801.

- [15] a) B. Basnet, M. Rajabi, H. Wang, P. Kumari, K. Thapa, S. Paul, M.O. Lavrentovich, O.D. Lavrentovich, Soliton walls paired by polar surface interactions in a ferroelectric nematic liquid crystal, *Nat. Commun.* 13 (2022) 3932, doi:10.1038/s41467-022-31593-w; b) P. Kumari, B. Basnet, H. Wang, O.D. Lavrentovich, Ferroelectric nematic liquids with conics, *Nat. Commun.* 14 (2023) 748, doi:10.1038/s41467-023-36326-1; c) N. Sebastián, M. Lovšin, B. Berteloot, N. Osterman, A. Petelin, R.J. Mandle, S. Aya, M. Huang, I. Drevenšek-Olenik, K. Neyts, A. Mertelj, Polarization patterning in ferroelectric nematic liquids via flexoelectric coupling, *Nat. Commun.* 14 (2023) 3029, doi:10.1038/s41467-023-38749-2; d) J. Yang, Y. Zou, W. Tang, J. Li, M. Huang, S. Aya, Spontaneous electric-polarization topology in confined ferroelectric nematics, *Nat. Commun.* 13 (2023) 7806, doi:10.1038/s41467-022-35443-7; e) P. Kumari, B. Basnet, M.O. Lavrentovich, O.D. Lavrentovich, Chiral ground states of ferroelectric liquid crystals, *Science* 83 (2024) 1364–1368, doi:10.1126/science.adl0834; f) J. Yang, Y. Zou, M. Huang, S. Aya, Flexoelectricity-driven toroidal polar topology in liquid-matter helielectrics, *Nat. Phys.* 20 (2024) 991–1000, doi:10.1038/s41567-024-02439-7.
- [16] M.T. Máthé, Á. Buka, A. Jákli, P. Salamon, Ferroelectric nematic liquid crystal thermomotor, *Phys. Rev. E* 105 (2022) L052701, doi:10.1103/PhysRevE.105.L052701.
- [17] a) S. Marni, G. Nava, R. Barboza, T.G. Bellini, L. Lucchetti, Walking ferroelectric liquid droplets with light, *Adv. Mater.* 35 (2023) 2212067, doi:10.1002/adma.202212067; b) M.T. Máthé, H. Nishikawa, F. Araoka, A. Jákli, P. Salamon, Electrically activated ferroelectric nematic microrobots, *Nat. Commun.* 15 (2024) 6928, doi:10.1038/s41467-024-50226-y.
- [18] a) M.T. Máthé, K. Perera, Á. Buka, P. Salamon, A. Jákli, Fluid ferroelectric filaments, *Adv. Sci.* 11 (2024) 2305950, doi:10.1002/advs.202305950; b) A. Jarosika, H. Nádasi, M. Schwidder, A. Manabe, M. Bremer, M.K. Memmer, A. Eremin, Fluid fibers in true 3D ferroelectric liquids, *Proc. Natl. Acad. Sci. U.S.A.* 121 (13) (2024) e2313629121, doi:10.1073/pnas.2313629121.
- [19] a) R. Barboza, S. Marni, F. Ciciulla, F.A. Mir, G. Nava, F. Caimi, T. Bellini, L. Lucchetti, Explosive electrostatic instability of ferroelectric liquid droplets on ferroelectric solid surfaces, *Proc. Natl. Acad. Sci. U.S.A.* 119 (32) (2022) e2207858119, doi:10.1073/pnas.2207858119; b) M.T. Máthé, B. Farkas, L. Péter, Á. Buka, A. Jákli, P. Salamon, Electric field-induced interfacial instability in a ferroelectric nematic liquid crystal, *Sci. Rep.* 13 (1) (2023) 6981, doi:10.1038/s41598-023-34067-1; c) S. Marni, F. Caimi, R. Barboza, N. Clark, T. Bellini, L. Lucchetti, Fluid jets and polar domains, on the relationship between electromechanical instability and topology in ferroelectric nematic liquid crystal droplets, *Soft Matter* 20 (25) (2024) 4878–4885, doi:10.1039/d4sm00317a.
- [20] F. Caimi, G. Nava, S. Fuschetto, L. Lucchetti, P. Paiè, R. Osellame, X. Chen, N.A. Clark, M.A. Glaser, T. Bellini, Fluid superscreening and polarization following in confined ferroelectric nematics, *Nat. Phys.* 19 (2023) 1658–1666, doi:10.1038/s41567-023-02150-z.
- [21] a) H. Nishikawa, F. Araoka, A new class of chiral nematic phase with helical polar order, *Adv. Mater.* 33 (2021) 2101305, doi:10.1002/adma.202101305; b) X. Zhao, J. Zhou, J. Li, J. Kougo, Z. Wan, M. Huang, S. Aya, Spontaneous helielectric nematic liquid crystals: electric analog to helimagnets, *Proc. Natl. Acad. Sci. U.S.A.* 118 (42) (2021) e2111101118, doi:10.1073/pnas.2111101118; c) C. Feng, R. Saha, E. Korblova, D. Walba, S.N. Sprunt, A. Jákli, Electrically tunable reflection color of chiral ferroelectric nematic liquid crystals, *Adv. Opt. Mater.* 9 (2021) 2101230, doi:10.1002/adom.202101230; d) J. Karcz, J. Herman, N. Rychłowicz, P. Kula, E. Górecka, J. Szydłowska, P.W. Majewski, D. Pocięcha, Spontaneous symmetry breaking in polar fluids, *Science* 384 (2024) 1096–1099, doi:10.1038/s41467-024-50230-2; e) C.J. Gibb, J. Hobbs, D.I. Nikolova, T. Raistrick, S.R. Berrow, A. Mertelj, N. Osterman, N. Sebastián, H.F. Gleeson, R.J. Mandle, Spontaneous symmetry breaking in polar fluids, *Nat. Commun.* 15 (2024) 5845, doi:10.1038/s41467-024-50230-2; f) H. Nishikawa, D. Okada, D. Kwaria, A. Nihonyanagi, M. Kuwayama, M. Hoshino, F. Araoka, Emergent ferroelectric nematic and heliconical ferroelectric nematic states in an achiral “straight” polar rod mesogen, *Adv. Sci.* 11 (2024) 2405718, doi:10.1002/advs.202405718.
- [22] X. Chen, V. Martinez, E. Korblova, G. Freychet, M. Zhernenkov, M.A. Glaser, C. Wang, C. Zhu, L. Radzihovsky, J.E. Maclennan, D.M. Walba, N.A. Clark, The smectic ZA phase: antiferroelectric smectic order as a prelude to the ferroelectric nematic, *Proc. Natl. Acad. Sci. U.S.A.* 120 (8) (2023) e2217150120, doi:10.1073/pnas.2217150120.
- [23] a) S.L. Qiu, M. Dutta, H.Z. Cummins, J.P. Wicksted, S.M. Shapiro, Extension of the Lifshitz-point concept to first-order phase transitions: incommensurate  $\text{NaNO}_2$  in a transverse electric field, 1986 *Phys. Rev. B*, 34 7901–7910, doi:10.1103/PhysRevB.34.7901; b) J.F. Scott, Prospects for ferroelectrics: 2012–2022, *Int. Sch. Res. Notices*, 2013, pp. 1–24, doi:10.1155/2013/187313.
- [24] a) J.P. Jamet, Electric field phase diagram of thiourea determined by optical birefringence, *J. Phys. Lett.* 42 (1981) 123–125, doi:10.1051/jphyslet:01981004206012300; b) P. Lederer, C.M. Chaves, Phase diagram of thiourea at atmospheric pressure under electric field: a theoretical analysis, *J. Phys. Lett.* 42 (1981) 127–130, doi:10.1051/jphyslet:01981004206012700.
- [25] E. Cruickshank, P. Rybak, M.M. Majewska, S. Ramsay, C. Wang, C. Zhu, R. Walker, J.M.D. Storey, C.T. Imrie, E. Gorecka, D. Pocięcha, To be or not to be polar: the ferroelectric and antiferroelectric nematic phases, *ACS Omega* 8 (2023) 36562–36568, doi:10.1021/acsomega.3c05884.
- [26] P. Nacke, A. Manabe, M. Klasen-Memmer, X. Chen, V. Martinez, G. Freychet, M. Zhernenkov, J.E. Maclennan, N.A. Clark, M. Bremer, F. Giesselmann, New examples of ferroelectric nematic materials showing evidence for the antiferroelectric smectic-Z phase, *Sci. Rep.* 14 (1) (2024) 4473, doi:10.1038/s41598-024-54832-0.
- [27] P.G. de Gennes, J. Prost, *The Physics of Liquid Crystals*, second ed., Oxford University Press, New York, 1993.
- [28] J. Fisher, A.G. Frederickson, Transport processes in anisotropic fluids II. coupling of momentum and energy transport in a nematic mesophase, *Mol. Cryst. Liq. Cryst.* 6 (2) (1969) 255–271, doi:10.1080/15421406908082963.
- [29] T.W. Spriggs, J.D. Huppler, R.B. Bird, An experimental appraisal of viscoelastic models, *Trans. Soc. Rheol.* 10 (1966) 191–213, doi:10.1122/1.549057.
- [30] a) P.T. Mather, D.S. Pearson, R.G. Larson, Flow patterns and disclination-density measurements in sheared nematic liquid crystals I: Flow-aligning 5CB, *Liq. Cryst.* 20 (5) (1996) 527–538, doi:10.1080/02678299608031139; b) P.T. Mather, D.S. Pearson, R.G. Larson, Flow patterns and disclination-density measurements in sheared nematic liquid crystals II: Tumbling 8CB, *Liq. Cryst.* 20 (5) (1996) 539–546, doi:10.1080/02678299608031140.
- [31] I.W. Stewart, *The Static and Dynamic Continuum Theory of Liquid Crystals: A Mathematical Introduction*, first ed., CRC Press, 2004, doi:10.1201/9781315272580.
- [32] a) K. Negita, S. Uchino, Rheological study on the shear-induced structural changes in liquid crystalline phases of octylcyanobiphenyl, *Mol. Cryst. Liq. Cryst.* 378 (1) (2002) 103–112, doi:10.1080/713738584; b) K. Negita, M. Inoue, S. Kondo, Dielectric study on the shear-induced structural changes in the nematic and the smectic-A phases of 4-n-octyl-4'-cyanobiphenyl (8CB), *Phys. Rev. E* 74 (2006) 051708, doi:10.1103/PhysRevE.74.051708; c) T. Yamamoto, Y. Nagae, T. Wakabayashi, T. Kamiyama, H. Suzuki, Calorimetry of phase transitions in liquid crystal 8CB under shear flow, *Soft Matter* 19 (2023) 1492–1498, doi:10.1039/d2sm01652d.
- [33] a) K. Szydłowska, P. Majewski, M. Čepič, N. Vaupotič, P. Rybak, C.T. Imrie, R. Walker, E. Cruickshank, J.M.D. Storey, P. Damian, E. Gorecka, Ferroelectric nematic-isotropic liquid critical end point, *Phys. Rev. Lett.* 130 (21) (2023) 216802, doi:10.1103/PhysRevLett.130.216802; b) M. Mrukiewicz, P. Perkowski, J. Karcz, P. Kula, Ferroelectricity in a nematic liquid crystal under a direct current electric field, *Phys. Chem. Chem. Phys.* 25 (2023) 13061, doi:10.1039/D3CP00714F; c) A. Adaka, P. Guragain, K. Perera, J. Nepal, R.J. Twieg, A. Jákli, Low field electrocaloric effect at isotropic–ferroelectric nematic liquid transition, *Soft Matter* 21 (2025) 458–462, doi:10.1039/D4SM00979G.
- [34] M.P. Kumar, J. Karcz, P. Kula, S. Karmakar, S. Dhara, Giant electroviscous effects in a ferroelectric nematic liquid crystal, *Phys. Rev. A* 19 (2023) 044082, doi:10.1103/PhysRevApplied.19.044082.
- [35] a) J. Thoen, G. Cordoyiannis, E. Korblova, D.M. Walba, N.A. Clark, W. Jiang, G.H. Mehl, C. Glorieux, Calorimetric evidence for the existence of an intermediate phase between the ferroelectric nematic phase and the nematic phase in the liquid crystal RM734, *Phys. Rev. E* 110 (2024) 014703, doi:10.1103/PhysRevE.110.014703; b) J. Thoen, G. Cordoyiannis, W. Jiang, G.H. Mehl, C. Glorieux, Phase transitions study of the liquid crystal DIO with a ferroelectric nematic, a nematic, and an intermediate phase and of mixtures with the ferroelectric nematic compound RM734 by adiabatic scanning calorimetry, *Phys. Rev. E* 107 (2023) 014701, doi:10.1103/PhysRevE.107.014701.
- [36] a) R.J. Hunter, J.V. Leyendekkers, Viscoelectric coefficient for water, *J. Chem. Soc. Faraday Trans. 1* 74 (1978) 450, doi:10.1039/F19787400450; b) D. Jin, Y. Hwang, L. Chai, N. Kampf, J. Klein, Direct measurement of the viscoelectric effect in water, *Proc. Natl. Acad. Sci. U.S.A.* 119 (1) (2022) e2113690119, doi:10.1073/pnas.2113690119.